Arabian Journal for Science and Engineering (2024) 49:15103–15119
https://doi.org/10.1007/s13369-024-08946-2

RESEARCH ARTICLE-MECHANICAL ENGINEERING

# A Computational Investigation of the Influence of Seafloor Conditions on the Turbulent Flow Characteristics of an Autonomous Underwater Vehicle

**Mahdi Tabatabaei Malazi[1] · Sergen Tumse[2] · Muammer Ozgoren[3] · Besir Sahin[2,4]**

Received: 20 October 2023 / Accepted: 10 March 2024 / Published online: 4 April 2024
© The Author(s) 2024

**Abstract**

The effect of the seabed on the hydrodynamics of three-dimensional autonomous underwater vehicles (AUVs) varies according to the physical conditions of the place where AUVs interact with the environmental conditions. This study examines the hydrodynamics of an AUV resembling a torpedo model while taking the influence of the seabed surface as a function of the dimensionless distances (*G/D*) between the torpedo and the seabed. Reynolds numbers, varying from $1 \times 10^4$ to $8 \times 10^4$, were considered. These Reynolds numbers were associated with various seabed distances falling within $0.25 \leq G/D \leq 1.5$. To perform the simulations, governing equations were utilized and incorporated with the k–ω SST turbulence model. It has been observed that when AUVs or torpedo models operate in close proximity to the seabed surface, several key hydrodynamic parameters and flow characteristics are affected. These include the pressure coefficient ($C_p$), drag coefficient ($C_D$), overall flow structures, maneuverability, and performance of the torpedo model. As the AUV or torpedo model approaches the seabed surface, the symmetrical flow pattern deteriorates. This deterioration is associated with changes in vortical flow structures under the influence of seabed surfaces. Additionally, the intensity of the shear stress ($\tau$) near the seabed surface gradually increases as the AUV or torpedo model gets closer to it. In summary, the proximity of AUVs or torpedo models to the seabed surface causes disruptions in the flow patterns, increased shear stress, and alterations in key hydrodynamic parameters, ultimately affecting the system's performance and behavior.

**Keywords** CFD · Hydrodynamic characteristics · Propulsive efficiency · Torpedo model · Turbulence models

## 1 Introduction

The use of underwater marine vehicles is growing steadily with the development of remote control and autonomous underwater vehicles (AUVs), which have become increasingly popular in multiple oceanographic applications [1, 2]. In addition, it is obligatory to determine what changes should be made in the design parameters in order to take the necessary measures for the protection of the AUVs that will sail close to the seabed during the seabed survey. The effect of the seabed on the hydrodynamics of AUVs varies according to the physical conditions of the place where the vehicle interacts. The AUV model was considered as the wingless torpedo-like geometry in the present study. Although the roughness of the seabed surface is very high, the AUV model discussed in this study is considered to travel on a flat surface, as it is a pioneer for future studies. In order to minimize the impact of the seabed on the AUVs' hydrodynamics, it is important to know the hydrodynamic structure of flow surrounding the AUV model. Therefore, an experimental study highlighted that investigations of the related hydrodynamic parameters and flow structures are indispensable, as hydrodynamic forces and related parameters substantially affect the AUVs' performance under deep underwater operation [3]. Their experimental studies based on the towing tank were

✉ Besir Sahin
besirsahin@aydin.edu.tr

1 Department of Mechanical Engineering, Faculty of Engineering, Istanbul Aydin University, 34295 Istanbul, Turkey

2 Department of Mechanical Engineering, Faculty of Engineering, Cukurova University, 01330 Adana, Turkey

3 Department of Aeronautical Engineering, Faculty of Aviation and Space Sciences, 42140 Konya, Turkey

4 Department of Aerospace Engineering, Faculty of Engineering, Istanbul Aydin University, 34295 Istanbul, Turkey

carried out at pitch angles ranging from 0° to 15° and at distinctive velocities of AUVs varying from 0.4 to 1.4 m/s. The experimental results revealed that a maximum increase in the normal force occurred compared to the axial force, especially at the highest velocity and angle of attack ($\alpha$). Alijani et al. [4] stated that the most influential parameters on the hydrodynamics of the AUVs' design are the nose, tail, blunt sections, and their dimensions. In numerical studies performed by Liu et al. [5], the LES method was employed to provide instantaneous flow data to reveal information about vortex control baffle mechanisms used to manage horseshoe vortices occurring around the sail of a DARPA SUBOFF model. They concluded that horseshoe vortices can permanently disappear passing over the tail of a submarine using efficient vortex control baffles. It is worth noting that undersea vehicles have several applications in diverse fields such as hydrology research, seabed exploration, oceanographic research, and beyond.

AUVs have begun to be used in areas occupied by undersea ice or similar seabed environments, particularly in Antarctica [6] and the Arctic regions [7]. Such areas are hazardous for AUVs [8]. In order to improve the hydrodynamic performance of underwater vehicles, it is important to conduct comprehensive analyses of the hydrodynamic properties of the geometric structure. The flow structure surrounding the main body and its components may significantly affect the maneuverability of underwater vehicles. In this case, deviations from the desired trajectory of the underwater vehicle may occur. In the optimization of hull design parameters, it is inevitable to consider the parameters that determine the hydrodynamic performance of the system. Essentially, the basis for establishing the design parameters of underwater vehicles lies in the comprehensive analysis of their hydrodynamic performance [9, 10]. The use of underwater vehicles (UWVs), including autonomous underwater vehicles (AUVs), in harsh and diverse environmental conditions has gained importance due to the increasing demand for shallow sea and deep ocean resources. These resources include research and extraction of seabed minerals, tracking of oxygen-secreting seagrasses, climatic monitoring for environmental conservation, research of hydrocarbons in deep-sea environments reaching depths of up to 6000 m, and many more.

Jadeh et al. [3] contributed to this field by developing a framework and conducting experimental research on the aerodynamic loads of an AUV Hull model. Their work aims to improve experiences and abilities regarding the hydrodynamic forces. It is substantially important for designers and practical engineers to have available knowledge about the lift coefficient ($C_L$), drag coefficient ($C_D$), and pitching moment coefficient ($M_\alpha$) that act on typical underwater vehicles. These investigations should cover various angles of attack ($\alpha$), velocities, and most importantly the height ratios ($G/D$) of underwater vehicles relative to the seabed. Here, the symbol $G$ indicates the distance from the bottom surface of the torpedo model to the seabed, and this distance is non-dimensionalized by the hull diameter ($D$) of the torpedo model. The most important situations, where underwater vehicles are affected or critical problems occur in terms of hydrodynamics conditions, often arise when they operate in proximity to the open sea surface or near the solid seabed surface. Moreover, the performance of the AUVs can be affected substantially when the yaw ($\beta$) and pitch angles ($\alpha$) change during the maneuvering action. For this reason, it is useful to review and study these critical situations of undersea vehicles. Sarigiguzel et al. [11] conducted an experimental study to understand the free sea surface that influences on the hydrodynamic structures around the torpedo model in a water channel. In this study, the height ($h$) from the central axis of the model to the water-free surface divided by the torpedo model hull diameter ($D$) was varied in the range of $0.50 \leq h/D \leq 3.50$. The model was submerged in the water in various positions. The free surface influences on the flow characteristics of the torpedo model with a chambered nose caused an antisymmetric wake domain downstream of the stern for the immerging range of $h/D \leq 1.0$. These flow structures were examined experimentally under zero angle of attack ($\alpha$) for Reynolds numbers varying between $\mathrm{Re} = 2 \times 10^4$ and $8 \times 10^4$. On the other hand, similar models and flow conditions were taken by Kilavuz et al. [12] into account to investigate flow characteristics by varying α between $0^0$ and $12^0$. It was found that particularly, on the upper shoulder of the stern, the separated flow domain was increased with a high rate of mixing process occurring between the main and separated flow domains. The conclusion derived by Kilavuz et al. [12] reveals that the free surface influences on the hydrodynamic parameters flow properties are negligible when $h/D$ is greater than 2.0. On the other hand, at the value of $h/d = 3.5$, the wake formed around the torpedo model becomes almost symmetrical [13].

Many creatures living under seawater have a low coefficient of friction ($f$) due to the geometrical shape of their general body structures. There are many creatures that can be considered as examples of innovative floating or flying vehicles. In this context, Stelle et al. [14] conducted an investigation into the drag forces ($F_D$) responsible for the deceleration of Steller sea lions during glide swimming. They measured the $F_D$ for 66 distinct glides performed by six juvenile sea lions and determined the associated drag coefficient ($C_D$) at a Reynolds number of $5.5 \times 10^5$ to be $C_D = 0.00568$. A larger nozzle diameter is recognized for its ability to enhance propulsion efficiency and enable faster swimming speeds in squid. With their incredibly streamlined aerodynamic body shape, these creatures can reach up to 11.1 m/s (40 km/h) speed in less than a second [15–18].

In the study of Tabatabaei Malazi [19], the design parameters of the squid model were optimized by employing the multi-objective genetic algorithm (MOGA) method and the response surface methodology. The primary goal of this optimization was to decrease the level of $F_D$ experienced by the modified squid model. Particularly, the real squid body exhibited a higher $F_D$ and related $C_D$ when compared to the modified squid model. This discrepancy in drag performance was attributed to the presence of a cavity around the body of the real squid, leading to an increased pressure drag force due to enlarged separation zones. Although many studies have been done on the vortical flow structures that occur during the travel or maneuver of undersea vehicles in a free-stream environment and close to the seawater surface, there is no research work available on the flow structures of those underwater vehicles or AUVs during their travel in the region close to the seabed surface. Similarly, it also affects the aerodynamic structure of the airfoil, slender, and non-slender delta wings during the landing and taking off duration or when those air vehicles fly close to the ground surface. However, it is possible to find few studies on the ground effects on the aerodynamics parameters of airfoils and various wings such as lift coefficient($C_L$), drag coefficient ($C_D$), pitching ($M_\alpha$), yawing ($M_\beta$), and rolling ($M_\phi$) moments as a function of angles of attack ($\alpha$) and Reynolds numbers [20–23].

The subject considered in the present work has distinct originality from previous studies examining the seabed influences on flow characteristics of AUVs similar to the torpedo model. Because the seabed surface influences are inevitably high over turbulent flow structures in the boundary layer region [24, 25]. The smaller ratio of $G/D$ indicating the distance between the torpedo model and the seabed surface causes a very low-pressure effect over the bottom wall of the model. Therefore, very low lift forces ($F_L$) took place due to the cylindrical shape and zero angle of attack ($\alpha$) of the model arrangement. Due to this reason, the $C_L$ has not been presented in this work.

### 1.1 Significance and Objective of the Work

The stability and navigational capability of the vehicle are highly dependent on the physical conditions of the surface of the seabed. The physical conditions of the seabed will greatly affect the navigational capability and stability of AUVs. Especially if the seabed surface contains sharp objects and jagged rocks, it becomes difficult to maintain the performance of the undersea vehicles at the desired level, and the probability of damage increases. Overall, understanding the seabed surface influences on underwater vehicles will enable them to operate safely and effectively and improve performance in harsh underwater environments. In this respect, in order to create a technological innovation in AUVs, it is inevitable to understand the effects of the physical structure

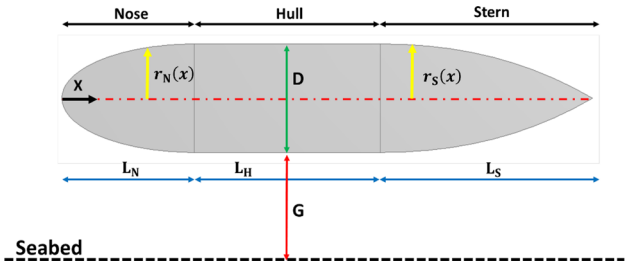



**Fig. 1** The schematic presentation of the Myring profile with certain parameters for the examined torpedo model

of the seabed on the hydrodynamic forces, travel parameters, maneuverability, and most importantly performance of the related AUVs or any other underwater vehicles. However, considering the disadvantages discussed here, the aim is to investigate the flow structures of AUVs or the torpedo model considered under the effect of the seabed surface. In order to observe the seabed effect, the change in the distance ($G$) between the torpedo model and the seabed surface was considered. The hydrodynamic design of the hull shape is a critical factor in the construction of an underwater vehicle, as it can significantly impact its flow resistance and overall performance.

As it is known in order to obtain the necessary information to reveal the effects of the seabed surface on the design parameters of the torpedo model, as shown in Fig. 1, the upstream part of the considered control volume, nose, hull, and stern dimensions and profiles of the torpedo model, as well as the downstream part of the considered control volume, must be taken into account.

## 2 Material and Method

In this study, a cylindrical body with an elliptical nose in the middle region and a gradually diverging tail geometry was created by Myring equations in order to examine the flow structures around a wingless torpedo model as an AUVs system. These equations were utilized in several studies, for example, please refer to [3, 9, 11, 26, 27]. The total length of the torpedo model as shown in Fig. 1 is taken as $L = 0.2$ m, and its diameter is $D = 0.04$ m. The dimensions of the detailed geometry of the model are, for example, nose length $L_N = 0.05$ m, hull length $L_H = 0.07$ m, and stern length $L_S = 0.08$ m. Profiles of the front and rear sections of the torpedo model such as profiles of nose and stern profiles were defined employing Eqs. (1) and (2). In other words, the profile of the nose and stern part of the modeling was designed according to the results of the calculations.

$$r_N(x) = \frac{1}{2}D\left[1 - \left(\frac{x - L_N}{L_N}\right)^2\right]^{\frac{1}{n}} \quad (1)$$

$$r_S(x) = \frac{1}{2}D - \left[\frac{3D}{2{L_S}^2} - \frac{\tan\theta}{L_S}\right](x - L_N - L_H)^2 + \left[\frac{D}{{L_S}^3} - \frac{\tan\theta}{{L_S}^2}\right](x - L_N - L_H)^3 \quad (2)$$

The angle $\theta$ in Eq. (1), which represents the model geometry of the submarine vehicle given schematically in Fig. 1, corresponds to the slope angle of the tail part of the model. The symbol $n$ represents the exponent of the parenthesis in Eq. (1). The tilt angle of the tail of the model, $\theta$, is taken as 30°. The slenderness ratio of the torpedo model was calculated as $L/D = 5$. It is worth mentioning that the variation range of the optimal slenderness ratio for the model, in general, was chosen as $4.15 \leq L/D \leq 6.3$ as suggested by Drew [28] and Karim et al. [29] in order to have an ogive-nosed geometry. However, the objective of incorporating an ogive-nosed geometry on the front face of the torpedo model is to minimize drag and enhance the overall performance of the torpedo.

## 2.1 Numerical Approach

This study focuses on the analysis of a flow that is steady, three-dimensional, incompressible, and turbulent. The equations of the Reynolds-averaged Navier–Stokes (RANS) can be expressed as follows:

Continuity equation:

$$\frac{\partial \rho}{\partial t} + \frac{\partial}{\partial x_i}(\rho \overline{u}_i) = 0 \quad (3)$$

Momentum equation:

$$\frac{\partial(\rho\overline{u}_i)}{\partial t} + \frac{\partial(\rho\overline{u}_i\overline{u}_j)}{\partial x_j} = -\frac{\partial \overline{p}}{\partial x_i} + \frac{\partial}{\partial x_j}\left[\mu\left(\frac{\partial \overline{u}_i}{\partial x_j} + \frac{\partial \overline{u}_j}{\partial x_i} - \frac{2}{3}\delta_{ij}\frac{\partial \overline{u}_l}{\partial x_l}\right)\right] + \frac{\partial}{\partial x_j}(-\rho\overline{u_i' u_j'}) \quad (4)$$

The term $-\rho\overline{u_i' u_j'}$ represents the Reynolds stresses.

The numerical analyses were conducted utilizing ANSYS Fluent commercial software in the simulation involved the application of the k–ω SST turbulence model, which was a combination of two models: the standard k–ω and the k–ε models [30]. The shear–stress transport (SST) k–ω model, which incorporates the shear–stress transport (SST) methodology, can be described by the following equations:

$$\frac{\partial}{\partial t}(\rho k) + \frac{\partial}{\partial x_i}(\rho k u_i) = \frac{\partial}{\partial x_j}\left(\Gamma_k \frac{\partial k}{\partial x_j}\right) + G_k + Y_k + S_k \quad (5)$$

$$\frac{\partial}{\partial t}(\rho\omega) + \frac{\partial}{\partial x_i}(\rho\omega u_i) = \frac{\partial}{\partial x_j}\left(\Gamma_\omega \frac{\partial \omega}{\partial x_j}\right) + G_\omega + Y_\omega + D_\omega + S_\omega \quad (6)$$

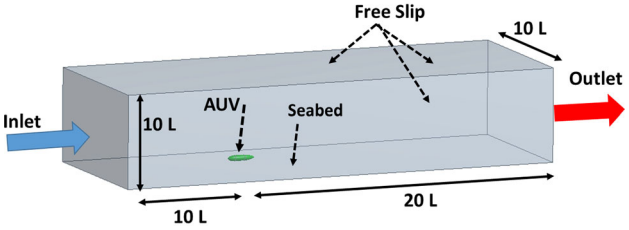



**Fig. 2** Schematic presentation of computational domain and boundary conditions

$$\Gamma_k = \mu + \frac{\mu_t}{\sigma_k} \text{and} \Gamma_\omega = \mu + \frac{\mu_t}{\sigma_\omega} \quad (7)$$

## 2.2 Numerical Approach, Boundary Conditions, and Mesh Details

A schematic image was shown to explain the boundary conditions and parameters of the computing domain in Fig. 2. Here, the AUV (Torpedo model) length (L) is taken as 0.2 m. Dimensions of the computational domain or control volume were chosen to be length = 30 L, height = 10 L, and width = 10 L, respectively. The AUV was positioned at 10 L downstream of the velocity inlet boundary and at 20 L upstream of the pressure outlet cross-section of the control volume. For the sides of the solution domain, a free slip boundary condition and, also for the wall bottom, a no-slip boundary condition were used. The incompressible water inflow into the control volume and the height between the water surface and the seabed is defined separately, and the outflow of the control volume is also defined.

The Reynolds number defined as Eq. (8) which was based on the characteristic length ($L$) of the model was employed to study the flow characteristics surrounding the torpedo model considered.

$$\text{Re} = \frac{\rho U L}{\mu} \quad (8)$$

where $\rho$, $U$, *and* $\mu$ present the water density, the free-stream velocity, and the dynamic viscosity of the fluid, respectively. There were a total of 20 various numerical simulation cases investigated. Four different Reynolds numbers such as $1.0 \times 10^4$, $2.0 \times 10^4$, $4.0 \times 10^4$, and $8.0 \times 10^4$ with four seabed dimensionless distances ($G/D = 0.25$, 0.5, 1, and 1.5) in the range of between 0.25 and 1.5 were considered. In addition, four simulations were carried out without the seabed effect for the purpose of comparisons.

Since the fluid and the model interact, the dimensions of the grid in close proximity to the model surface have been taken very small in order to minimize the error rate in the

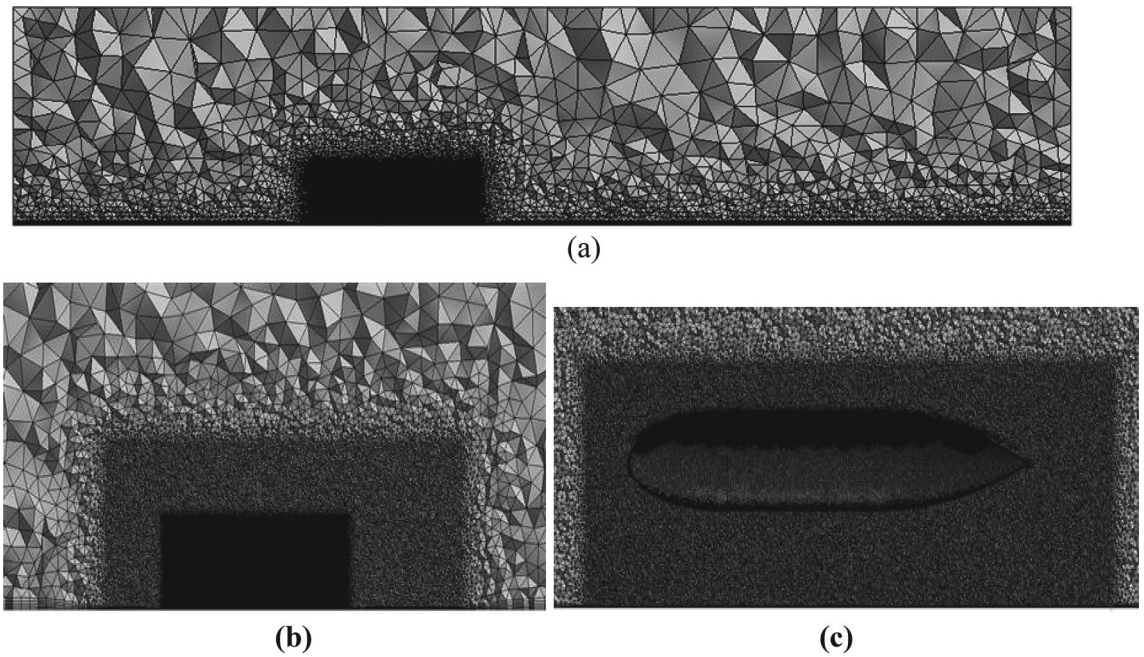



**Fig. 3** Presentations of mesh distributions with different conditions: **a** detailed mesh distributions, **b** mesh distributions in a certain focused area around the AUV model, and **c** a focused plan view of mesh distributions near the AUV model

calculation. In addition, much attention has been paid to the periphery of the model, particularly around the stern part due to the high possibility of the boundary layer detachment. To predict the fluid flow properties, the combined pressure-based algorithm and the SIMPLE (Semi-implicit method for pressure-related equations) scheme were chosen. Convergence criterion level was chosen as $10^{-6}$ for the governing equations, and the necessary checks were made in order to ensure correct results under the current flow conditions. The three-dimensional governing equations were solved until they met the predefined minimum convergence criterion while considering the specified boundary and input conditions. The computational domain included tetrahedron and prism elements for meshing, with the inclusion of high-density mesh along the walls to enhance the accuracy of the results.

As indicated in Fig. 3, 35 million cells were used for the calculation area. A study on mesh independence was carried out for the computational domain. Table 1 shows how the drag coefficient ($C_D$) varies with different elements. The element numbers demonstrated in Table 1 are utilized for mesh independence study, and it is clear that $35 \times 10^6$ elements give sufficiently accurate results with an error value of 0.38%. It was also observed that around 35 million elements could be employed to effectively solve the adjusted torpedo model across different Reynolds numbers with an error of nearly 0.38%. The thickness of the first layer was modified to ensure that the y + value was less than 1 for all runs.

**Table 1** Results of the mesh independence study

| Mesh resolution | Drag coefficient | % difference |
|---|---|---|
| $16 \times 10^6$ elements | 0.1979 | 28.50 |
| $20 \times 10^6$ elements | 0.1855 | 20.45 |
| $25 \times 10^6$ elements | 0.1694 | 10.00 |
| $30 \times 10^6$ elements | 0.1611 | 4.60 |
| $32 \times 10^6$ elements | 0.1555 | 0.97 |
| $35 \times 10^6$ elements | 0.1546 | 0.38 |
| $40 \times 10^6$ elements | 0.1540 | 0 |

The data as shown in Fig. 4 reveal that the percentage error between the mesh elements of $35 \times 10^6$ and $40 \times 10^6$ is only 0.38%. Consequently, the mesh comprising $35 \times 10^6$ elements is considered for the remaining simulations in this article.

The data presented in Table 2 give a brief summary of the numerical simulations conducted in the present work. In order to reveal the accuracy of the numerical predictions, a comparison was performed between the drag coefficient ($C_D$) values obtained in the present investigation and those reported in a previous study available in the literature, in order to validate the findings. Table 3 presents the drag coefficient ($C_D$) values obtained at two different Reynolds numbers under free-stream conditions. The obtained drag coefficient ($C_D$) results reveal a remarkable similarity.

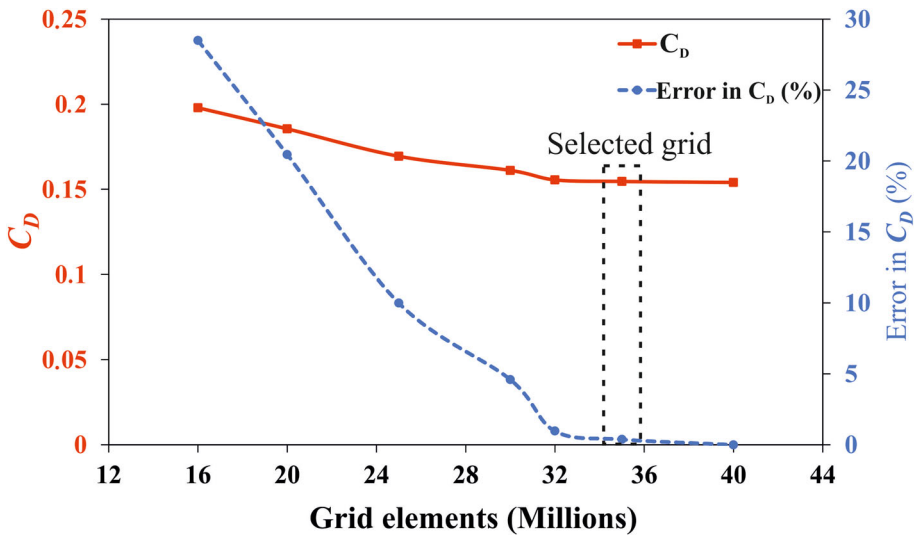



**Fig. 4** Mesh reliability test including the change of the drag coefficient ($C_D$) at different grid elements

**Table 2** The range of numerical simulations conducted in the present investigation

| G/D | Reynolds number (Re) |
|---|---|
| 0.25, 0.5, 1, 1.5 | $1.0 \times 10^4$, $2.0 \times 10^4$, $4.0 \times 10^4$, $8.0 \times 10^4$ |
| Without G/D | $1.0 \times 10^4$, $2.0 \times 10^4$, $4.0 \times 10^4$, $8.0 \times 10^4$ |

**Table 3** Comparison of drag coefficient ($C_D$) results predicted in the present work with the literature at Re = $2.0 \times 10^4$ and $4.0 \times 10^4$

| Reynolds numbers | Present study | Kilavuz et al. [31] |
|---|---|---|
| $2.0 \times 10^4$ | 0.2445 | 0.2447 |
| $4.0 \times 10^4$ | 0.1825 | 0.1889 |

## 3 Numerical Results and Discussion

### 3.1 Flow Hydrodynamics Surrounding the Torpedo Model

Just like the navigation of underwater vehicles in the area close to the seabed, the flight of aircraft during takeoff and landing stages or close to the ground is one of the most critical situations. While unmanned and other aircrafts with slender and non-slender delta wings fly near the ground/sea surfaces, aerodynamic parameters and vortical flow structures vary significantly compared to the free-stream region in other words far from the ground surface [32–34]. Two-thirds of the world is water. Therefore, human beings have always wondered about the biological structure of the sea and ocean seabed surface. In this context, they have started to conduct several research works on the bottom of the sea with AUVs. In summary, it is beneficial to produce data for designers and practitioners by examining the hydrodynamic structure of AUVs during their movement in the region close to the seabed surface, as in aircraft traveling close to the earth's surface.

Figures 5 and 6 show the distribution of dimensionless time-averaged velocity component ($< u/U_\infty >$) with the color scale, with *G/D*, for a range of $2 \times 10^4 \leq \mathrm{Re} \leq 8 \times 10^4$. Naturally, the separated flow region formed on the tail of the model as shown in Fig. 6 has a symmetrical structure due to the existence of the free-stream conditions. However, when the torpedo model approaches the seabed surface, the symmetrical structure of the separated flow region formed around the tail and downstream of the model begins to deteriorate. For example, in the case of the torpedo model positioned at $G/D = 1$, where the torpedo model's bottom surface approaches the seabed surface, it is evident that the boundary layer detaches from the torpedo model's surface at an earlier stage compared to its upper surface. This unsymmetrical wake formation somehow decreases with further decreasing the ratio of *G/D*. As can be seen from the color scale, the value of the velocity component ($< u/U_\infty >$) decreases with the decrease in the dimensionless distance *G/D* between the torpedo model and the seabed surface. As it is known, the velocity vector magnitude gradually decreases with the effect of shear stress as the model's bottom wall approaches the seabed in the vertical plane.

Figures 7 and 8 illustrate that the seabed effects on the patterns of the time-averaged vertical dimensionless velocity component ($< v/U_\infty >$) at Re = $2 \times 10^4$ and Re = $4 \times 10^4$ have a plus sign on the upper surface and have a minimum sign from the bottom surface of the model toward the seabed plane. The time-averaged velocity component ($< v/U_\infty >$) in the vertical direction shows similar variations compared to the streamwise time-averaged velocity component ($< u/U_\infty >$) in the free-stream region, that is, there

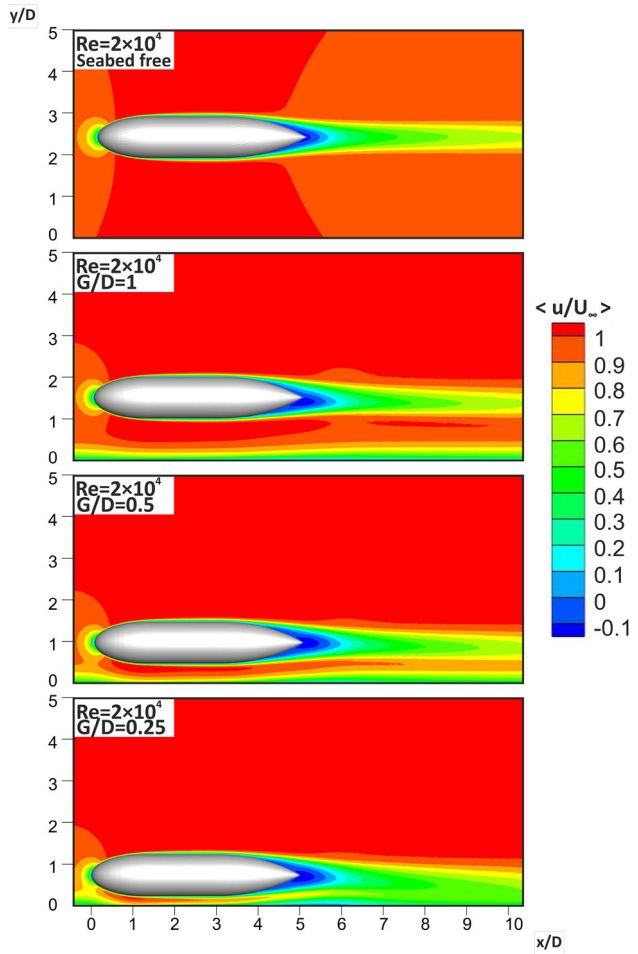



**Fig. 5** The seabed effect on the patterns of dimensionless velocity component (< $u/U_\infty$ >) at Re = 2 × $10^4$

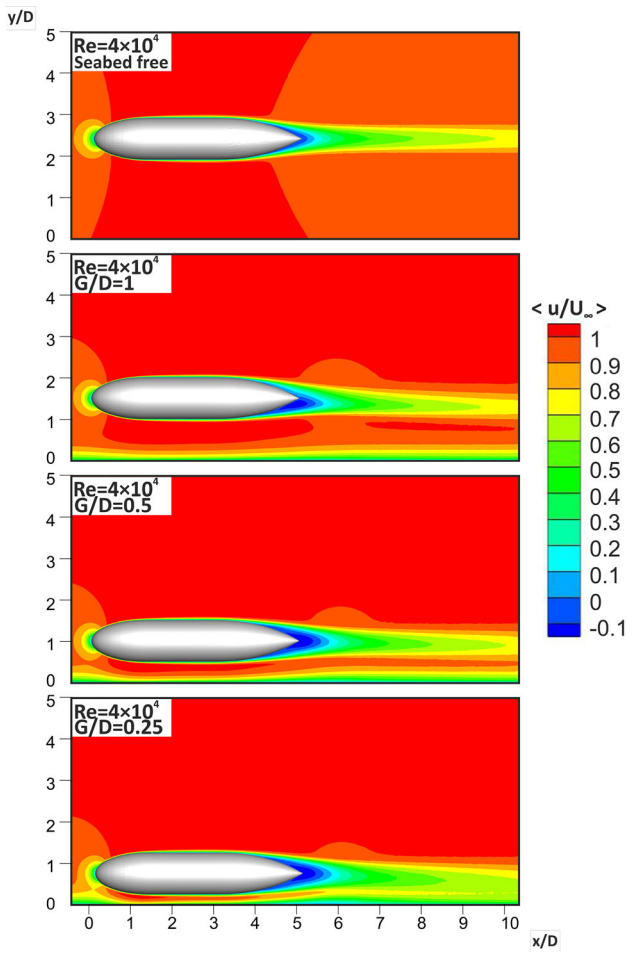



**Fig. 6** The seabed effect on the patterns of dimensionless velocity component (< $u/U_\infty$ >) at Re = 4 × $10^4$

is no seabed effect, a symmetrical flow structure is formed around the tail part of the torpedo model. However, if the model is located in the boundary layer region, the seabed surface influence on behaviors of the flow increases as the *G/D* ratio decreases. The averaged velocity component (< $v/U_\infty$ >) in the vertical direction shows these variations in vortical flow structures more clearly compared to the patterns of the streamwise time-averaged velocity component (< $u/U_\infty$ >).

Figures 9 and 10 demonstrate the combination of time-averaged streamline (< $\Psi$ >) pattern and dimensionless vorticity distribution (< $\omega D/U_\infty$ >) for 2 × $10^4$ ≤ Re ≤ 4 × $10^4$.

In the region with no seabed effect, that is, in the free-stream region, the separated flow region around the model trail edge covers a very small area. The length of the wake extends up to the merging point of core flows. This point is also called the saddle point and is denoted by the symbol*S*. More specifically, core flow around geometry merges at the saddle point (*S*) developing a stagnation point. However, when the ratio of G/*D* is reduced, the model emerges into the boundary layer region, and the hydrodynamics of the model start to receive the effect of the shear stress more since the bottom surface model approaches the seabed surface. The length between the rear edge of the tail and the saddle point *S* gets larger. As the model gets closer to the seabed surface, the velocity values due to the shear stress decrease, and therefore, the local Reynolds number also decreases. Thus, the expansion wake flows also increase because the momentum of the fluid elements moving along the shear layers surrounding the model deteriorates while the local Reynolds number is decreased.

The objective of this study is to provide a comprehensive and improved understanding of the hydrodynamic and physical aspects of the flow. To achieve this, an isosurface representation of the flow was employed, allowing vortical flow structures surrounding the torpedo model and turbulent coherent structures within the wake region to be quantitatively examined. As previously mentioned, the torpedo model was longitudinally positioned in the horizontal plane, near the seabed, to meticulously observe the influence of the

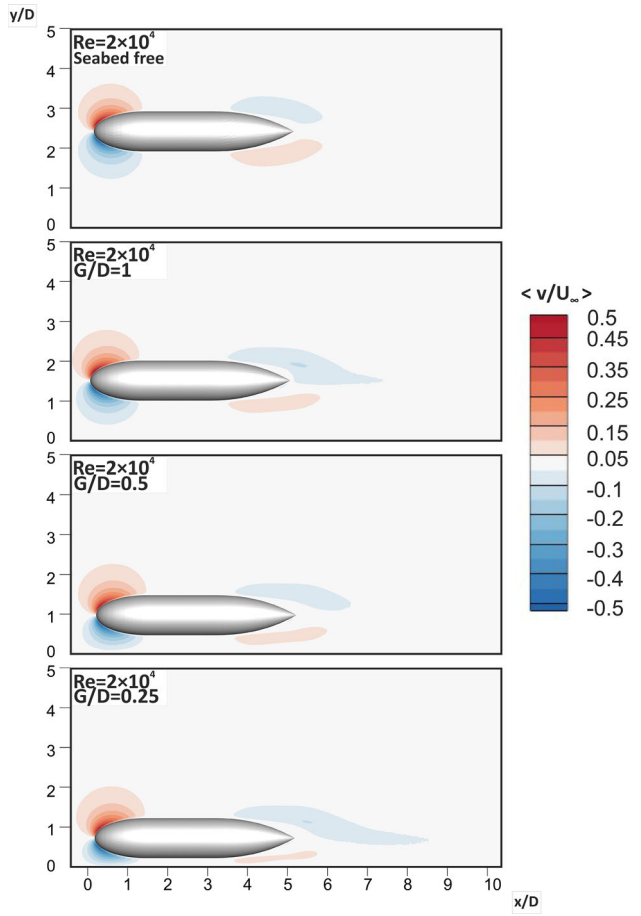



**Fig. 7** The seabed effect on the patterns of vertical velocity component ($< v/U_\infty >$) at Re $= 2 \times 10^4$

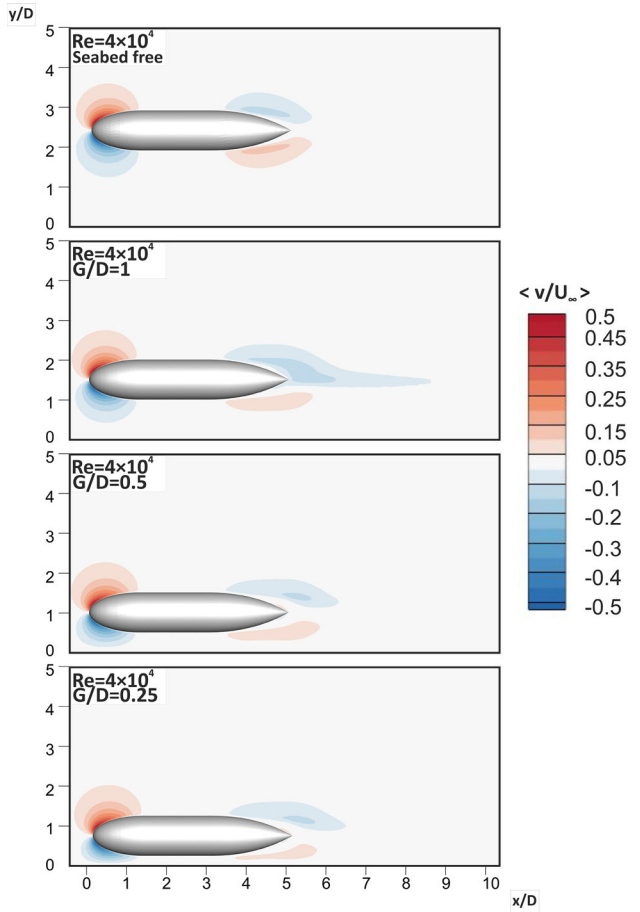



**Fig. 8** The seabed effect on the patterns of vertical velocity component ($< v/U_\infty >$) at Re $= 4 \times 10^4$

seabed surface during numerical analysis, which was conducted using the k–ω SST turbulence model.

The nose and stern sections of the torpedo model exhibit three-dimensional geometric variations, which are of significant importance in the development of chaotic flow structures within a 3D coordinate system. Additionally, the formation of a 3D wake region especially occurs around the periphery of 3D geometries which are also influenced by various factors of flow structures. These factors include the constrained flow area between the bottom wall of the torpedo model and the seabed surface, the effects of hydrodynamic buoyancy forces, and the presence of the detached flow structures, particularly at the periphery of the stern section. The patterns of ($< \Psi >$) for $G/D = 0.25$ and 0.50 in Fig. 9 clearly show the separated flow region with a limited circulation around the trailing section of the model. Consequently, the interaction between these reversed flows and the stern's surface, in conjunction with all the aforementioned parameters, contributes to the enhancement of three-dimensional flow structures with high turbulent intensity. Furthermore, it is evident that the 3D flow, characterized by the stretching of well-defined vorticity structures due to the seabed effect, exhibits variations with different $G/D$ ratios, as demonstrated by the isosurface presentation in Figs. 11 and 12. These figures illustrate the diversity of 3D stretching vortical flow structures around the periphery of the stern under the seabed effect, depending on the isosurface of the Q-criterion at percent-level magnitudes of (i) 0.02, (ii) 0.03, (iii) 0.04 for Re $= 2 \times 10^4$, and Re $= 4 \times 10^4$, respectively. The Q-criterion data are presented in Figs. 12 and 13, including the maximum Q-criterion magnitudes, along with the intensity levels of normalized time-averaged vorticity ($< \omega D/U_\infty >$). Moreover, numerical animations have revealed that flow patterns within the wake inherently undergo chaotic changes, thereby enhancing the development of 3D vortical flow structures. The interaction between eddies developed in the wake regions and the model boundary is more pronounced within the range of $G/D \leq 0.75$. The Q-criterion fraction is determined by utilizing the expression, $Q = 0.5 \times (\|\omega\|^2 - \|S\|^2)$, where $Q > 0$ indicates the dominance of rotating terms over the stretching component in fluid element deformation as reported by

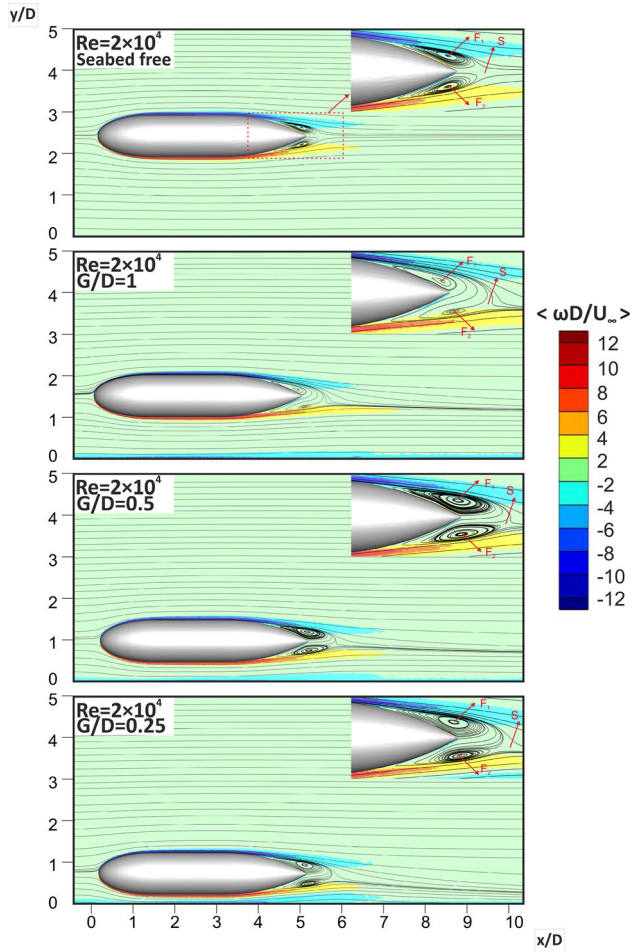



**Fig. 9** The seabed effect on the patterns of streamlines (< $\Psi$ >) and vorticity distributions (< $\omega D/U_\infty$ >) for Re = 2 × $10^4$

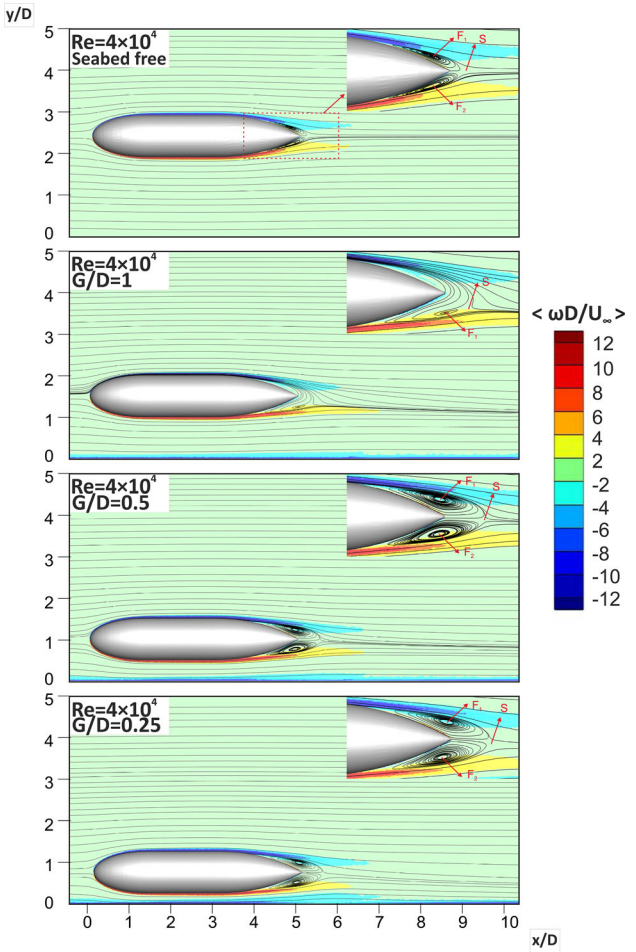



**Fig. 10** The seabed effect on the patterns of streamline (< $\Psi$ >) and vorticity distribution (< $\omega D/U_\infty$ >) for Re = 4 × $10^4$

Anonymous [35]. Examining multiple data of the Q-criterion with varied orders of magnitude proves to be valuable for comparison. As shown in Figs. 11 and 12, higher Q-criterion values cause larger-scale swirling concentrations in vortical flow structures, while a low level of the Q-criterion causes over-dispersion of smaller-scale swirling fluid concentration in the vortical flow structures.

The resulting presentations of the Q-criteria isosurface reveal that for all $Q$ values such as 0.02, 0.03, and 0.04, well-defined vorticity concentrations wrap the model and do not change the shape while rolling around the periphery of the model further downstream without splitting into small-scale swirling fluid bubbles at the rear of the stern in the case of $Q =$ 0.04 when the torpedo model is immersed in the free-stream. The resulting presentation of the $Q$-criterion isosurface and the extraction of well-defined vortical flow structures efficiently demonstrate the 3D vorticity concentrations at a percentage of $Q = 0.02$. This is depicted in the second and third rows of images for $G/D = 1.0$ and 0.5. Deformed swirling fluid concentrations begin to appear around the periphery of the torpedo model. As these swirling and rolling fluid concentrations move downstream of the torpedo, they split into smaller-scale swirling fluid bubbles due to the influence of the seabed surface. As the $G/D$ ratio decreases, these flow structures become more pronounced. Turbulent shear flows are generally dominated by unsteady flow, while three-dimensional spatially coherent and time-dependent swirling flow surrounding the torpedo model are often called coherent structures [31]. When the $G/D$ parameter of the torpedo model gets smaller, the vortical flow structure becomes asymmetrical as the torpedo model approaches the seabed surface. For example, in the case of $G/D = 0.25$, the deformed vorticity concentrations start to roll by interacting with the upper surface of the torpedo model, and these randomly formed rolling flow structures after the stern of the model breaks up and form small-size rolling flow bubbles. As the Q value gets smaller, as shown in the fourth row of Figs. 11 and 12, the number of these rolling flow bubbles starts to decrease. The formation of small-scale vorticity bubbles and the evolutionary dynamic nature of these bubbles increases the energy

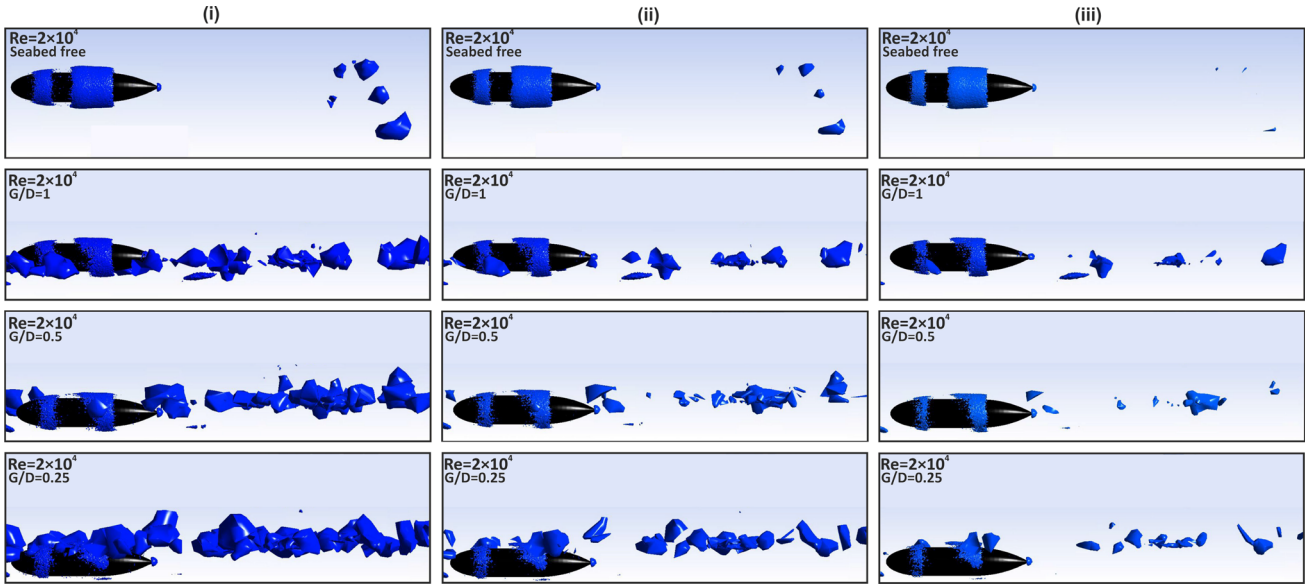



**Fig. 11** Presentations of three-dimensional stretching vorticity concentrations over the torpedo model under the influence seabed surface for the Q-criterion of (**i**) 0.02, (**ii**) 0.03, and (**iii**) 0.04 at Re $= 2 \times 10^4$

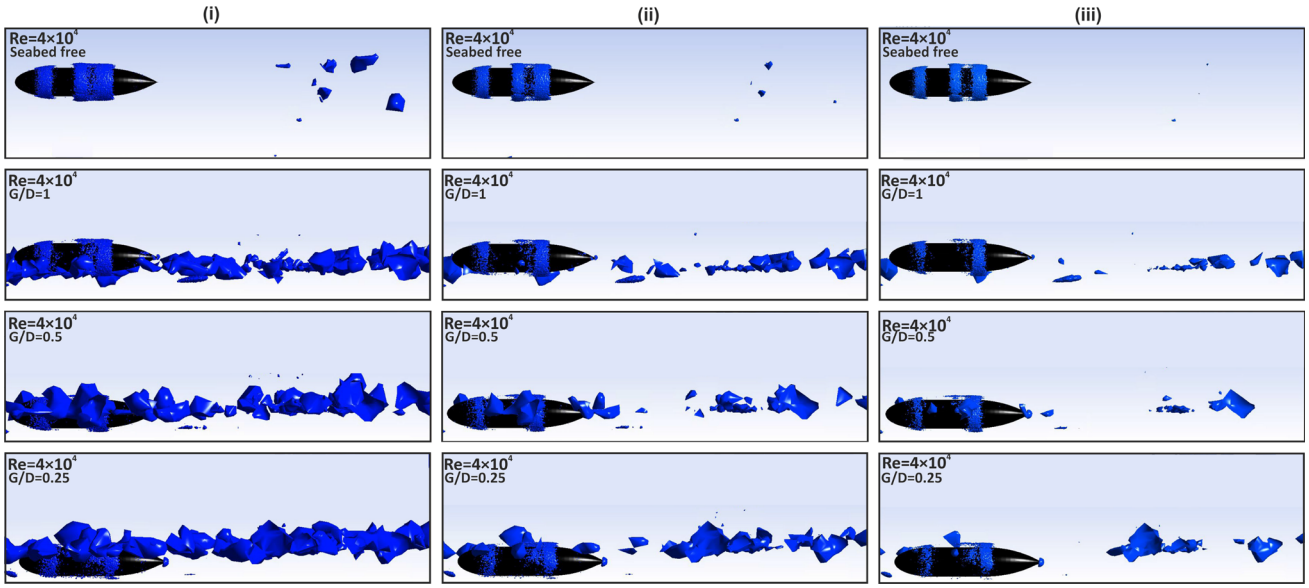



**Fig. 12** Presentations of three-dimensional stretching vorticity concentrations over the torpedo model under the influence seabed surface for the Q-criterion of (**i**) 0.02, (**ii**) 0.03, and (**iii**) 0.04 at $Re = 4 \times 10^4$

density in the main trace region around the stern and in the long-distance path regions.

## 3.2 The Seabed Effect on Distributions of Pressure Coefficient

Variations of pressure coefficient ($C_P$) all around the surfaces of the torpedo along the vertical symmetry axis for $G/D = 1$, 0.5, and 0.25 as well as seabed free case at Re $= 2 \times 10^4$ and Re $= 4 \times 10^4$ are shown in Figs. 13 and 14, respectively.

To more specifically explain the effects of immersion ratio, G/D, as well as Reynolds numbers against hydrodynamics of flow surrounding the torpedo model, the distributions $C_P$ over the AUV geometry or torpedo model are demonstrated in Fig. 13. As stated by Subburaj et al. [36], the hydrostatic pressure ($P_h$), is assumed to balance the buoyancy force acting on the torpedo body. To eliminate the buoyancy effects, the hydrostatic pressure ($P_h$) is subtracted from the piezometric pressure ($P_{piez}$) to find out static pressure ($P_\infty$) at the inlet cross-section of the control volume as shown in Eq. (9). This

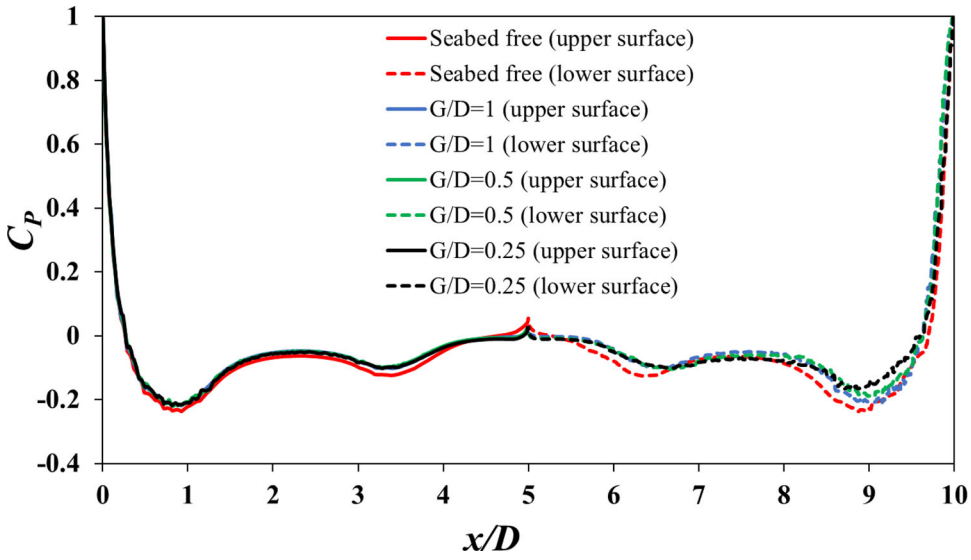



**Fig. 13** Variations of pressure coefficient ($C_P$) along the top and bottom surfaces of the torpedo model for $G/D = 1$, 0.5, and 0.25 as well as seabed free case at Re $= 2 \times 10^4$

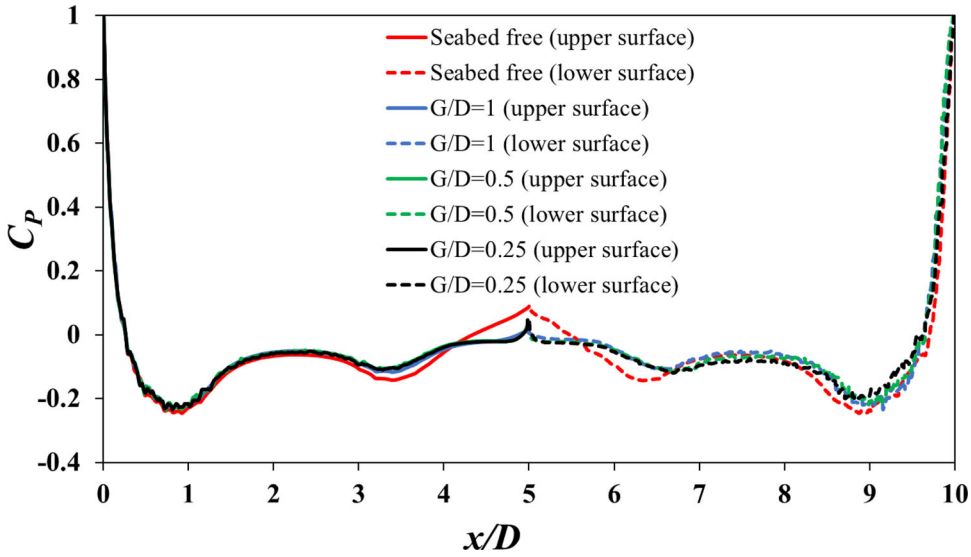



**Fig. 14** The pressure coefficient ($C_P$) distributions at the top and bottom surfaces of the torpedo model for $G/D = 1$, 0.5, and 0.25 as well as seabed free case at Re $= 4 \times 10^4$

approach yields the distribution of the pressure coefficients ($C_p$) presented in Fig. 13.

$$C_P = \frac{Ps - (P_{\text{piez}} - P_h)}{\frac{1}{2}\rho U_\infty^2} = \frac{Ps - P\infty}{\frac{1}{2}\rho U_\infty^2} \tag{9}$$

Similar observations have been recorded by Das et al. [37] and Kilavuz et al. [31]. The maximum $C_P$ occurs at the stagnation point on the torpedo model nose where the stagnation pressure takes place, and as the fluid flows in the vicinity of the elliptical nose with an increased velocity, the $C_p$ gets a negative value with maximum magnitude about the locations of $x/D = -1$ on the upper wall of the torpedo model, considering all ratios of $G/D$. Conversely, on the lower surface, regardless of the $G/D$ cases, the maximum negative value of $C_P$ also reoccurs around the location at $x/D = 1$. The pressure coefficient ($C_P$) variations along the top wall of the model as a function of $G/D$ exhibit nearly identical values to the free-stream case. However, along the lower wall of the model, the $C_P$ values show approximately 30% changes around the location of $x/D = 1$ compared to the free-stream results at Re $= 4 \times 10^4$. The $C_P$ variations at the same locations rise by 40% for Reynolds number of $2 \times 10^4$. Notably, the $C_p$ values for the free-stream or seabed free case are consistently higher than those observed under the seabed effect ($G/D$) for both Reynolds numbers.

### 3.3 The Seabed Effect on the Drag Coefficient

The intensity of the drag force ($F_D$) generally changes with Reynolds numbers according to the geometrical shape of the object and the magnitude of the force impacts on the object moving in the fluid or exposed to the flow. Therefore, the torpedo model was taken into account in these studies

to reduce the drag resistance as much as possible. (Please see also; Tabatabaei Malazi [16]; Batchelor [38]; Olcay and Tabatabaei Malazi et al., [39]. The $F_D$ of the torpedo model in the case of undersea operations is determined by utilizing Eq. (10).

$$F_D = F_{D_\text{pressure}} + F_{D_\text{viscous}} = \oint P\hat{n}.\hat{e}_d dS + \oint \tau_w \hat{t}.\hat{e}_d dS \tag{10}$$

where $F_{D_\text{pressure}}$ is the pressure drag, $F_{D_\text{viscous}}$ is the viscous drag, $p$ is the pressure and $\tau$ is the wall share stress. The total $F_D$ is needed to be determined to define the drag coefficient ($C_D$) presented in Eq. (11).

$$C_D = \frac{F_{\text{Drag}}}{\frac{1}{2}\rho U^2 A} \tag{11}$$

Here, $F_{\text{Drag}}$ is the total drag force, $\rho$ is the density of the fluid,$U$ is the free-stream velocity of the fluid, and $A$ is the projected area of the torpedo model.

It is worth mentioning that the validation of the current numerical study concerning the drag coefficient ($C_D$) was found to be in complete agreement with the numerical analysis conducted by Kilavuz et al. [31], as demonstrated in Table 3, while both studies considered the same torpedo model geometry under free-stream condition.

Figure 15 shows the total drag coefficient ($C_D$) based on the total drag forces ($F_D$) of the torpedo model. It is worth mentioning that viscous drag forces do not differ significantly with and without seabed effects, but pressure drag forces differ substantially while the distance *G/D* is reduced. As the torpedo model approaches the seabed surface, the lift force ($F_L$) increase is ignorable because of zero angle of attack ($\alpha$).

Figure 15 presents the drag coefficient ($C_D$) under the seabed effect for Reynolds numbers Re $= 2 \times 10^4$, $4 \times 10^4$ and other *Re*. As shown in the figure, as the *G/D* level decreases, in other words, as the bottom wall of the torpedo model approaches the seabed surface, the Reynolds number of the flow to which the model is exposed also decreases. For this reason, the drag coefficient ($C_D$) of the flow also changes as a function of *G/D*, and as the value of *G/D* decreases, the $C_D$ value inversely increases compared to the free-stream case. In general, if the bottom wall of the model is 4D above the seabed surface, it is seen that the drag coefficient ($C_D$) value stabilizes at $4 \times 10^4$ of the Reynolds number. Cross comparison of the all Reynolds numbers and *G/D* ratios demonstrates that the $C_D$ values have similar decrement trends while increasing both G/D ratios and Reynolds numbers.

### 3.4 Determination of Impulse Power Under the Seabed Effect

The geometry of a solid body that is in motion or interacting with the flow in the external flow environment is very important in terms of aerodynamics or hydrodynamics forces. Therefore, underwater vehicles are designed to minimize drag force ($F_D$). While these sensitivities are considered in the torpedo-like geometry analyzed in this study, it remains crucial to investigate how the flow structure to which the model is exposed may alter when traveling in close proximity to the seabed surface. The primary purpose of this study is to determine the variations of the thrust force ($F_T$) moving the system by calculating the hydrodynamic forces under the seabed effect.

### 3.5 Definition of Water Jet Velocities and Thrust Force

Sufficient thrust force ($F_T$) is needed for underwater vehicles to continue their journey with constant acceleration. When underwater or air vehicles are moving in the horizontal plane, it is necessary to produce a thrust force ($F_T$) above the force equivalent to the fluid resistance that they are exposed to, in other words, hydrodynamic forces. Although the thrust force ($F_T$) is generated by different methods in order to counter the drag force ($F_D$) that AUVs or any other underwater vehicles are exposed by fluid resistance, it is anticipated that the necessary thrust force ($F_T$) required for the AUVs/underwater vehicles is obtained by the transformation of high-pressure water into kinetic energy. A very fast-moving torpedo underwater is also possible using a water jet propulsion system. In addition, it is possible to ensure the movement of the system at very low speeds by controlling the thrust force ($F_T$) created by the water jet. During steady-state fluid flow, it was determined that the thrust force ($F_T$) responsible for propelling the torpedo model equals the drag force ($F_D$) exerted by the surrounding water. Furthermore, the numerical estimation of the drag force ($F_D$) acting on the torpedo model was also numerically analyzed. That is, the thrust forces ($F_T$) are also calculated using three-dimensional continuity and momentum equations [16, 19, 40]. However, the thrust force ($F_T$) of the water jet can be calculated using one-dimensional momentum equations such as;

$$F_T = \rho A_{\text{jet}} u_{\text{jet}} (u_{\text{jet}} - u_{\text{vehicle}}) \tag{12}$$

where $\rho$ is the fluid density, $A_{\text{jet}}$ is the cross-sectional area of the water jet, $U_{\text{jet}}$ is the average velocity of the water jet, and $U_{\text{vehicle}}$ is the torpedo model speed. The values of $A_{\text{jet}}$ were defined to be 1.9635E-05 $m^2$, 7.85E-05 $m^2$, and 3.14E-04 $m^2$ for the nozzle diameters of 0.005 m, 0.01 m, and 0.02 m, respectively. The equation mentioned earlier builds

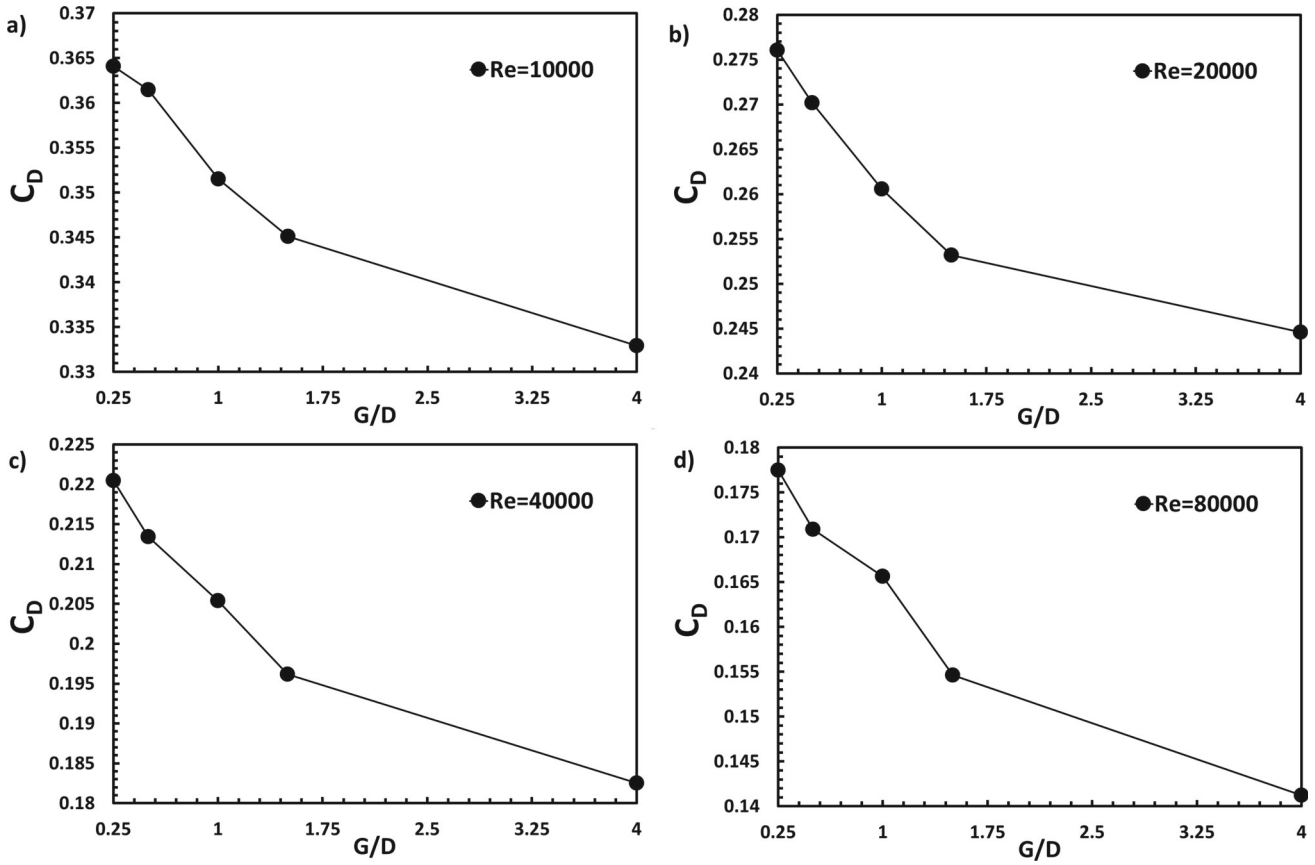



**Fig. 15** The seabed effect on the drag coefficient ($C_D$) of the torpedo model at Reynolds numbers (Re): **a** $1 \times 10^4$, **b** $2 \times 10^4$, **c** $4 \times 10^4$, and **d** $8 \times 10^4$

a relationship between the thrust force, water jet, and torpedo velocities. Once the thrust force is obtained, the calculation of the required water speed for different torpedo speeds can be completed.

Figure 16 reveals normalized waterjet velocity ($U_{jet}$) released from the stern of the torpedo without and with the seabed effect as a function of the Reynolds number as well as nozzle diameter. The waterjet velocity is non-dimensionalized dividing the jet velocity ($U_{jet}$) by the AUV speed ($U_{AUV}$). The non-dimensional waterjet velocity exhibited a reduction of almost 62%, 60%, 58%, and 56% when the non-dimensional nozzle diameter ($D_{nozzle}/D$) shifted from 0.122 to 0.5 for the torpedo with $Re = 1 \times 10^4, 2 \times 10^4, 4 \times 10^4$, and $8 \times 10^4$. When the dimensionless nozzle diameter ($D_{nozzle}/D$) is reduced while keeping the other parameters of the control volume constant, the velocity of the dimensionless waterjet ($U_{jet}/U_{AUV}$) naturally increases due to the conservation of mass. If the cross-section area of the nozzle exit gets smaller, the waterjet velocity ($U_{jet}/U_{AUV}$) must then increase to compensate for the reduced cross-section area of this nozzle exit and the volume flow rate of the waterjet must remain constant according to the continuity equation. In addition, if the torpedo model gradually approaches the seabed surface, the velocity of the dimensionless waterjet increases ($U_{jet}/U_{AUV}$) as the *G/D* ratio decreases. For example, when the $D_{nozzle}/D$ ratio drops to a value of 0.125, the waterjet velocity ratio ($U_{jet}/U_{AUV}$) increases by approximately 8% for $Re = 8 \times 10^4$ and $D_{nozzle}/D = 0.125$ when *G/D* changes from 0.25 to 1.5 values.

### 3.6 Waterjet Propulsive Efficiency

It is substantially important to investigate the propulsion efficiency of waterjets in underwater vehicle movements. For example, the low noise level of submarine vehicles, in general, is important, as well as the operating range and related limitations of the parameters that increase the performance and maneuverability of underwater vehicles. For example, if the mechanism that creates the waterjet is embedded in the body of the vehicle, it may lower the noise generated by the mechanisms of the waterjet system. The separation occurring around the periphery of the nose part of the torpedo model can be eliminated by water suction at a proper location in the forward face of AUVs. On the other hand, the waterjet released from the proper locations of the stern part of the AUV can eliminate the wake developed around the

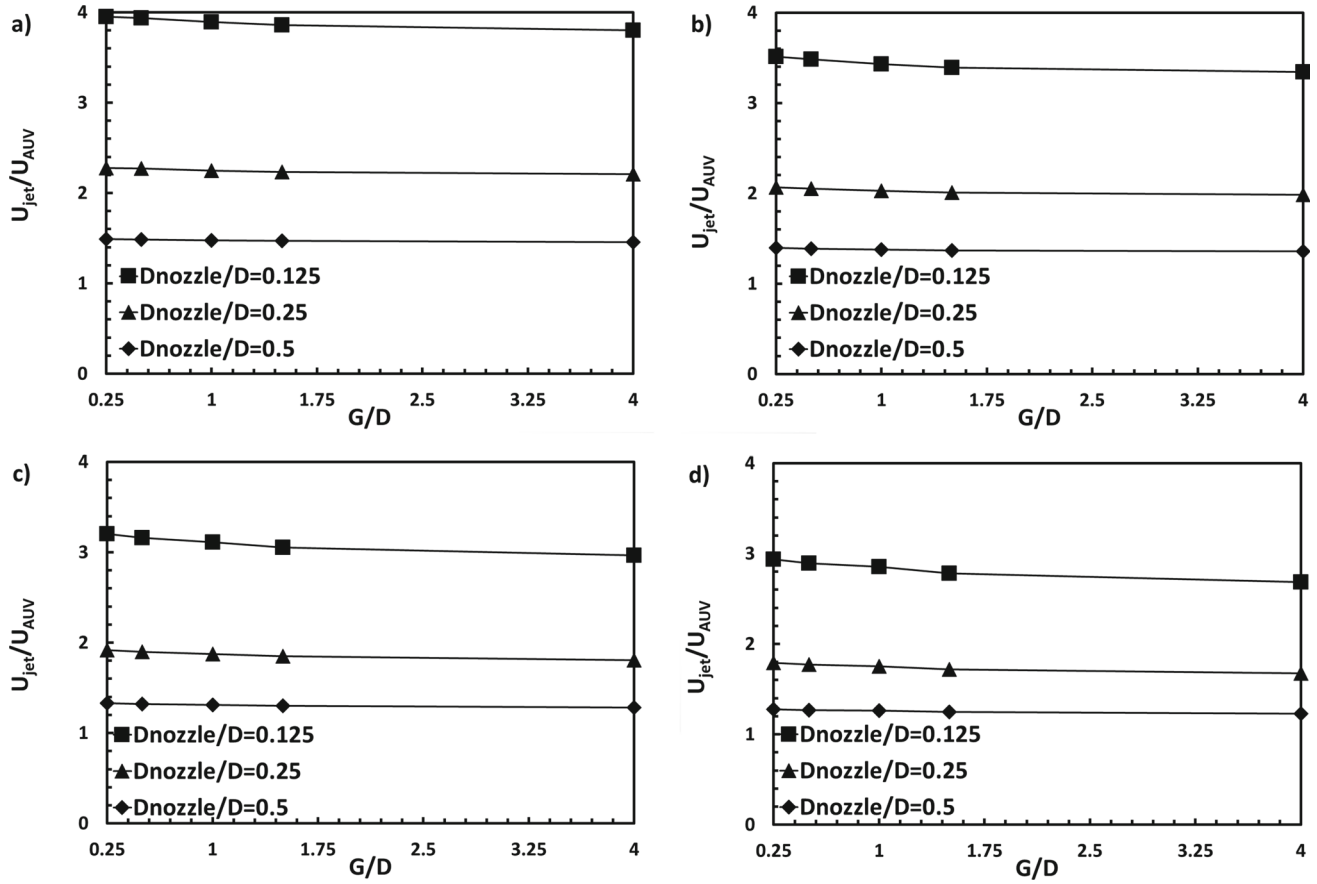



**Fig. 16** Variations of dimensionless waterjet velocity ($U_{jet}/U_{AUV}$) with *G/D* ratios, for Reynolds numbers (Re): **a** $1 \times 10^4$, **b** $2 \times 10^4$, **c** $4 \times 10^4$, and **d** $8 \times 10^4$ at various normalized nozzle diameters

periphery of the stern due to the suction process to reduce the drag force ($F_D$) caused by the water flow resistance. When the waterjet is realized from the torpedo model exit, without having the waterjet swirling and lowering the magnitude of separations may also increase the system performance. The waterjet propulsion efficiency ($\eta_p$) is defined as:

$$\eta p = \frac{2}{1 + U_{jet}/U_{vehicle}} \tag{13}$$

This parameter of efficiency is based on velocities, such as the waterjet mean velocity ($U_{jet}$) and mean $U_{AUV}$ speed. The mean value of $U_{jet}$ was determined at various traveling average speeds of the AUV and nozzle diameters; the associated waterjet propulsive efficiencies ($\eta_p$) were obtained. Figure 17 represents the variations of waterjet propulsive efficiency ($\eta_p$) of the torpedo model which has the Myring profile constructed by Eqs. (1) and (2). As seen from the waterjet propulsive efficiency ($\eta_p$), it increases slightly as a function of *Re*. Furthermore, the propulsion exhibited an increase of almost 98%, 88%, 80%, and 72% when the non-dimensional nozzle diameter shifted from 0.122 to 0.5 for the torpedo model with $Re = 1 \times 10^4, 2 \times 10^4, 4 \times 10^4$, and $8 \times 10^4$.

The propulsive efficiency ($\eta_p$) rises with an increase in the nozzle diameter. Consequently, the optimum waterjet propulsive efficiency ($\eta_p$) is achieved when the largest dimensionless nozzle diameter, $D_{nozzle}/D = 0.5$, is employed.

## 4 Conclusions

It is clear that the seabed affects the hydrodynamic parameters of the underwater vehicles during the journey close to the seabed surface. For example, the maneuverability of a torpedo model considered in this study will be affected during its voyage for research and exploration near the surface of the seabed**.** The system will be exposed to the yaw ($\beta$), pitch ($\alpha$), and rolling angles ($\phi$) during maneuvering, and hence, more unsymmetrical flow structures form around the tail part of the system. In summary, the flow structure surrounding the system affects the hydrodynamic forces and characteristics that the system is exposed to. Therefore, in this study, the hydrodynamic forces along with the structure

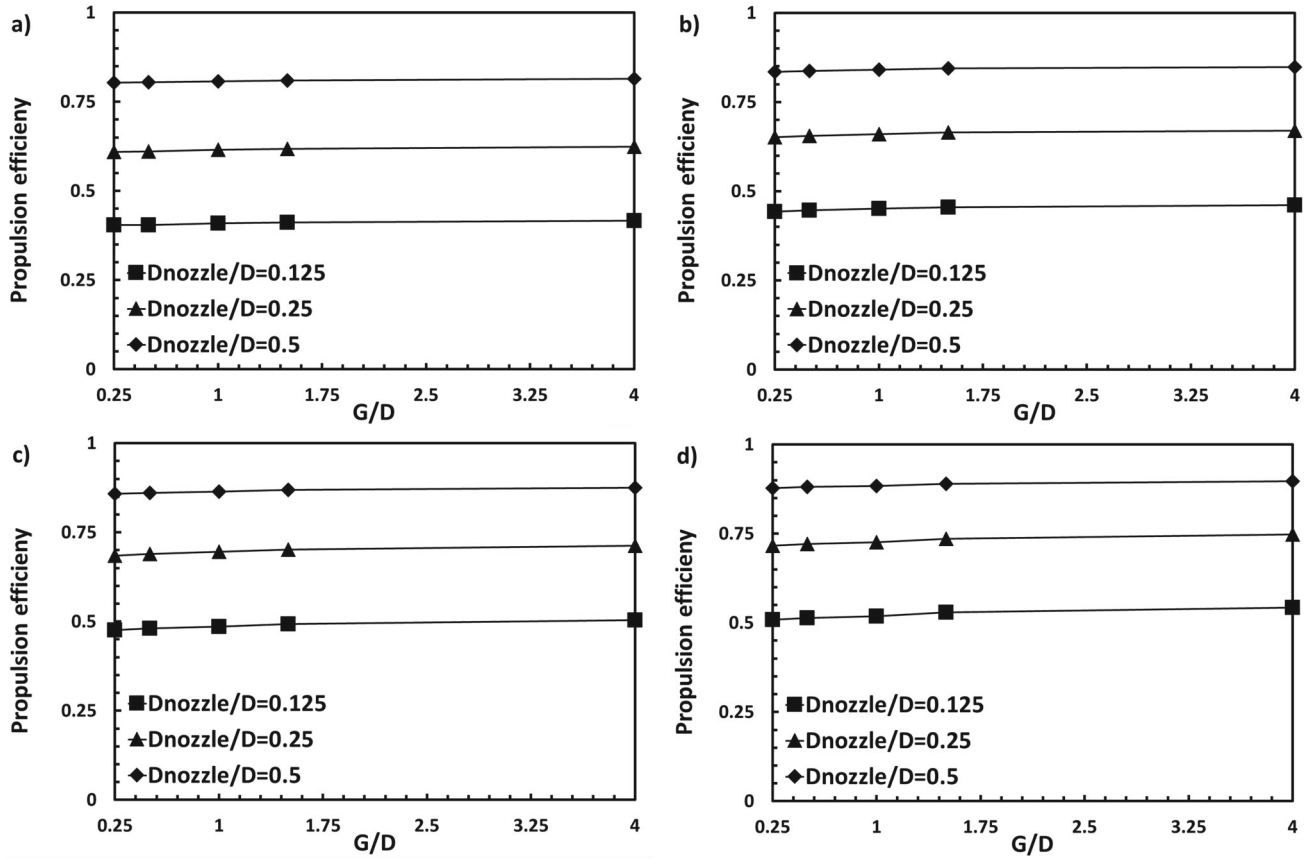



**Fig. 17** Variations of waterjet propulsive efficiency ($\eta_p$) based on *G/D* ratios for Reynolds numbers (Re): **a** $1 \times 10^4$, **b** $2 \times 10^4$, **c** $4 \times 10^4$, and **d** $8 \times 10^4$ at various normalized nozzle diameters

of the flow were also examined, and the pressure coefficient ($C_p$), drag coefficient ($C_D$), dimensionless waterjet velocity ($U_{jet}/U_{AUV}$), and propulsive efficiency ($\eta_p$) were predicted.

The simulation employs the k–ω SST turbulence model integrating the standard k–ω model with the k–ε model to solve the fundamental equations. These equations, derived from the Reynolds-averaged Navier–Stokes (RANS) equations, are three-dimensional. Numerical results indicate that when the torpedo model operates near the seabed surface, several parameters are influenced. These include the lift and drag forces acting on the system, the flow patterns surrounding the torpedo model, as well as the overall locomotion, maneuverability, and efficiency of the torpedo model.

When the torpedo model approaches the seabed surface, the symmetrical structure of the separated flow region formed around the tail and downstream of the model begins to deteriorate. For example, in the present torpedo model positioned at a location of $G/D = 1$, it is seen that the boundary layer is halted from the model wall at an earlier stage compared to its upper surface. However, it has been observed that if the AUVs or torpedo model moves in close proximity to the seabed surface, the pressure coefficient ($C_p$), the drag coefficient ($C_D$) of the system, the flow structure surrounding the system, its movement, and maneuverability are affected. The drag coefficient ($C_D$) values exhibit comparable decrement tendencies as both *G/D* and Reynolds number increase as shown by a cross-comparison of all the impacts of Reynolds numbers and *G/D* values. The symmetrical structure of the separated flow zone around the tail and downstream of the torpedo model begins to deteriorate. The intensity of the increasing shear stress ($\tau$) in the region close to the seabed surface gradually increases influencing other flow parameters, especially the time-averaged velocity components ( $< u/U_\infty >$, $< v/U_\infty >$) which vary as a function of *G/D*. As the momentum of the fluid elements moving along the surrounding shear layers weakens, the length of the separated flow region increases.

The waterjet propulsive efficiency ($\eta_p$) rises with an increase in the nozzle diameter ($D_{nozzle}$). Consequently, the optimum waterjet propulsive efficiency ($\eta_p$) is achieved when the largest dimensionless nozzle diameter, $D_{nozzle}/D = 0.5$, is employed.

Investigation of drag and vibration-reducing modifications, additions of new components, and mechanisms play an essential role in the development and future of the UUVs by increasing their fuel and speed efficiency along with lowering vibration to minimize disturbances of tracked marine life

and sonar camouflage. Over the past decade, there has also been great interest in applying rough surfaces while mimicking the properties of various animals, such as shark skin, dolphin skin, and muscle vibrations, in marine drag reduction applications within the scope of passive flow control methods [41]. For future studies, active flow control methods can be applied to reduce the seabed effects and flow separation on the torpedo-like geometry. Techniques such as suction, blowing, and synthetic jets can be strategically applied to the nose and afterbody sections. Additionally, passive flow control methods can complement these efforts by modifying the nose, fuselage, and stern geometry sections. The incorporation of winglets (wings/flaps/airfoils) around the geometry, particularly focusing on the stern section, further enhances the effectiveness of these flow control measures. These flow control methods collectively contribute to delaying flow separation, reducing the drag coefficient, and improving maneuvering capabilities. Additionally, a comprehensive experimental study can be conducted in the future to further investigate and validate numerical predictions.

**Acknowledgements** One of the authors, Dr. Muammer Ozgoren, would like to thank the Turkish Technological Research Council (TÜBİTAK) for its support to the project numbered 214M318.

**Funding** Open access funding provided by the Scientific and Technological Research Council of Türkiye (TÜBİTAK).

**Data availability** Data will be made available on request.

## Declarations

**Conflict of interest** The authors declare that they have no known competing financial interests or personal relationships that could have appeared to influence the work reported in this paper.

**Open Access** This article is licensed under a Creative Commons Attribution 4.0 International License, which permits use, sharing, adaptation, distribution and reproduction in any medium or format, as long as you give appropriate credit to the original author(s) and the source, provide a link to the Creative Commons licence, and indicate if changes were made. The images or other third party material in this article are included in the article's Creative Commons licence, unless indicated otherwise in a credit line to the material. If material is not included in the article's Creative Commons licence and your intended use is not permitted by statutory regulation or exceeds the permitted use, you will need to obtain permission directly from the copyright holder. To view a copy of this licence, visit http://creativecommons.org/licenses/by/4.0/.

## References

1. Das, B.; Subudhi, B.; Pati, B.B.: Cooperative formation control of autonomous underwater vehicles: an overview. Int. J. Autom. Comput. **13**, 199–225 (2016)
2. An, D.; Mu, Y.; Wang, Y.; Li, B.; Wei, Y.: Intelligent path planning technologies of underwater vehicles: a review. J. Intell. Robot. Syst. **107**, 22 (2023)
3. Jagadeesh, P.; Murali, K.; Idichandy, V.G.: Experimental investigation of hydrodynamic force coefficients over AUV hull form. Ocean Eng. **36**, 113–118 (2009)
4. Alijani, M.; Zeinali, M.; Nouri, N.M.: Designing of the body shape of an autonomous underwater vehicle using the design of Experiments Method. Proc. Inst. Mech. Eng. C J. Mech. Eng. Sci. **233**, 6307–6325 (2018)
5. Liu, G.; Hao, Z.; Bie, H.; Wang, Y.; Ren, W.; Hua, Z.: Control mechanism of a vortex control baffle for the horseshoe vortex around the sail of a DARPA SUBOFF model. Ocean Eng. **275**, 114166 (2023)
6. Jenkins, A.; Dutrieux, P.; Jacobs, S.S.; McPhail, S.D.; Perrett, J.R.; Webb, A.T.; White, D.: Observations beneath pine island glacier in west Antarctica and implications for its retreat. Nat. Geosci. **3**, 468–472 (2010)
7. Dowdeswell, J.A.; Evans, J.; Mugford, R.; Griffiths, G.; McPhail, S.; Millard, N.; Stevenson, P.; Brandon, M.A.; Banks, C.; Heywood, K.J.; Price, M.R.; Dodd, P.A.; Jenkins, A.; Nicholls, K.W.; Hayes, D.; Abrahamsen, E.P.; Tyler, P.; Bett, B.; Jones, D.; Wadhams, P.; Wilkinson, J.P.; Stansfield, K.; Ackley, S.: Autonomous underwater vehicles (auvs) and investigations of the ice–ocean interface in Antarctic and Arctic Waters. J. Glaciol. **54**, 661–672 (2008)
8. Chen, X.; Bose, N.; Brito, M.; Khan, F.; Thanyamanta, B.; Zou, T.: A review of risk analysis research for the operations of autonomous underwater vehicles. Reliab. Eng. Syst. Saf. **216**, 108011 (2021)
9. Gao, T.; Wang, Y.; Pang, Y.; Cao, J.: Hull shape optimization for autonomous underwater vehicles using CFD. Eng. Appl. Comput. Fluid Mech. **10**, 599–607 (2016)
10. Joung, T.-H.; Sammut, K.; He, F.; Lee, S.-K.: Shape optimization of an autonomous underwater vehicle with a ducted propeller using computational fluid dynamics analysis. Int. J. Naval Arch. Ocean Eng. **4**, 44–56 (2012)
11. Sarigiguzel, F.; Kilavuz, A.; Ozgoren, M.; Durhasan, T.; Sahin, B.; Kavurmacioglu, L.A.; Akilli, H.; Sekeroglu, E.; Yaniktepe, B.: Experimental investigation of free-surface effects on flow characteristics of a torpedo-like geometry having a cambered nose. Ocean Eng. **253**, 111174 (2022)
12. Kilavuz, A.; Sarigiguzel, F.; Ozgoren, M.; Durhasan, T.; Sahin, B.; Kavurmacioglu, L.A.; Akilli, H.; Sekeroglu, E.; Yaniktepe, B.: The impacts of the free-surface and angle of attack on the flow structures around a torpedo-like geometry. Eur. J. Mech. B. Fluids **92**, 226–243 (2022)
13. Kilavuz, A.; Durhasan, T.; Ozgoren, M.; Sarigiguzel, F.; Sahin, B.; Kavurmacioglu, L.A.; Akilli, H.; Sekeroglu, E.; Yaniktepe, B.: Influence of free-surface on wake flow characteristics of a torpedo-like geometry. J. Mar. Sci. Technol. **27**, 1130–1147 (2022)
14. Stelle, L.L.; Blake, R.W.; Trites, A.W.: Hydrodynamic drag in Steller sea lions (*Eumetopias jubatus*). J. Exp. Biol. **203**, 1915–1923 (2000)
15. Tabatabaei, M.M.; Okbaz, A.; Olcay, A.B.: Numerical investigation of a longfin inshore squid's flow characteristics. Ocean Eng. **108**, 462–470 (2015)
16. Olcay, A.B.; Malazi, M.T.: The effects of a longfin inshore squid's fins on propulsive efficiency during underwater swimming. Ocean Eng. **128**, 173–182 (2016)
17. Tabatabaei Malazi, M.; Olcay, A.B.: Investigation of a longfin inshore squid's swimming characteristics and an underwater locomotion during acceleration. Appl. Ocean Res. **55**, 76–88 (2016)
18. Olcay, A.; Tabatabaei, M.; Okbaz, A.; Heperkan, H.; Fırat, E.; Ozbolat, V.; Gökçen, M.; Sahin, B.: Experimental and numerical investigation of a longfin inshore squid's flow characteristics. J. Appl. Fluid Mech. **10**, 21–30 (2017)
19. Tabatabaei Malazi, M.: Design optimization of a longfin inshore squid using a genetic algorithm. Ocean Eng. **279**, 114583 (2023)
20. Tumse, S.; Tasci, M.O.; Karasu, I.; Sahin, B.: Effect of ground on flow characteristics and aerodynamic performance of a non-slender Delta Wing. Aerosp. Sci. Technol. **110**, 106475 (2021)

21. Deng, N.; Agarwal, R.K.: Numerical simulation of DLR-F6 wing-body flow field in ground effect. Comput. Fluids **245**, 105576 (2022)
22. Srinidhi, N.G.; Vengadesan, S.: Ground effect on tandem flapping wings hovering. Comput. Fluids **152**, 40–56 (2017)
23. Wu, J.; Qiu, Y.L.; Shu, C.; Zhao, N.; Wang, X.: An adaptive immersed boundary-lattice Boltzmann method for simulating a flapping foil in ground effect. Comput. Fluids **106**, 171–184 (2015)
24. Ozgoren, M.; Okbaz, A.; Dogan, S.; Sahin, B.; Akilli, H.: Investigation of flow characteristics around a sphere placed in a boundary layer over a flat plate. Exp. Thermal Fluid Sci. **44**, 62–74 (2013)
25. Hayder, M.A.; Goktepeli, I.; Yagmur, S.; Ozgoren, M.; Kose, F.; Kavurmacioglu, L.A.: Experimental investigation of flow structures around a torpedo-like geometry placed in a boundary layer flow. Univ. J. Mech. Eng. **6**, 1–8 (2018)
26. Shi, Y.; Pan, G.; Yan, G.-X.; Yim, S.C.; Jiang, J.: Numerical study on the cavity characteristics and impact loads of AUV water entry. Appl. Ocean Res. **89**, 44–58 (2019)
27. Saghafi, M.; Lavimi, R.: Optimal design of nose and tail of an autonomous underwater vehicle hull to reduce drag force using numerical simulation. Proc. Inst. Mech. Eng. Part M J. Eng. Maritime Environ. **234**, 76–88 (2019)
28. Drew, B.A.: Measurement methods and analysis: Forces on Underwater Gliders. (2002).
29. Karim, M.M.; Rahman, M.M.; Alim, M.A.: Performance of SST k-w turbulence model for computation of viscous drag of axisymmetric underwater bodies. Int. J. Eng. **24**(2), 139–146 (2011)
30. Menter, F.R.: Two-equation eddy-viscosity turbulence models for engineering applications. AIAA J. **32**, 1598–1605 (1994)
31. Kilavuz, A.; Ozgoren, M.; Kavurmacioglu, L.A.; Durhasan, T.; Sarigiguzel, F.; Sahin, B.; Akilli, H.; Sekeroglu, E.; Yaniktepe, B.: Flow characteristics comparison of PIV and numerical prediction results for an unmanned underwater vehicle positioned close to the free surface. Appl. Ocean Res. **129**, 103399 (2022)
32. Tasci, M.O.; Tumse, S.; Sahin, B.: Vortical flow characteristics of a slender delta wing in ground effect. Ocean Eng. **261**, 112120 (2022)
33. Tasci, M.O.; Tumse, S.; Sahin, B.: The impact of the ground on flow structure and aerodynamic characteristics of a double delta wing. Aerosp. Sci. Technol. **130**, 107943 (2022)
34. Tumse, S.; Karasu, I.; Sahin, B.: Experimental investigation of ground effect on the vortical flow structure of a 40° swept Delta Wing. J. Aerosp. Eng. **35**, 04022055 (2022)
35. Anonymous, 2022b. https://www.m4-engineering.com/q-criterion-for-vortex-visualization/ (Accessed on 13 March 2022).
36. Subburaj, R., Khandelwal, P., Vengadesan, S.: Numerical study of flow past an elliptic cylinder near a free surface. Phys. Fluids. 30, (2018).
37. Das, H.N.; Rao, N.; Suman, K.N.S.; Prasad, V.V.S.: Performance prediction of elliptical head form profile of a submerged body. J. Inst. Eng. **86**, 46–49 (2006)
38. Batchelor, G.K.: An introduction to fluid dynamics. Cambridge University Press, UK (2000)
39. Tabatabaei Malazi, M.; Eren, E.T.; Luo, J.; Mi, S.; Temir, G.: Three-dimensional fluid–structure interaction case study on Elastic Beam. J. Marine Sci. Eng. **8**, 714 (2020)
40. Moslemi, A.A.; Krueger, P.S.: Propulsive efficiency of a biomorphic pulsed-jet underwater vehicle. Bioinspir. Biomim. **5**, 036003 (2010)
41. Fu, Y.F.; Yuan, C.Q.; Bai, X.Q.: Marine drag reduction of shark skin inspired Riblet surfaces. Biosurf. Biotribol. **3**, 11–24 (2017)